DOI: https://doi.org/10.12442/j.issn.1002-185X.20250358.

Dynamic tensile deformation mechanisms of $Fe_{40}Mn_{20}Cr_{20}Ni_{20}$ high-entropy alloys at cryogenic temperatures

Junwei Qiao[a,b,1], **Zeming Wang**[a], **Yong Zhang**[c], **Peter K. Liaw**[d]

[a]*College of Materials Science and Engineering, Taiyuan University of Technology, Taiyuan 030024, China*

[b]*Key Lab of Interface Science and Engineering in Advanced Materials, Ministry of Education, Taiyuan University of Technology, Taiyuan 030024, China*

[c]*Beijing Advanced Innovation Center of Materials Genome Engineering, State Key Laboratory for Advanced Metals and Materials, University of Science and Technology Beijing, Beijing 100083, China*

[d]*Department of Materials Science and Engineering, the University of Tennessee, Knoxville, TN 37996-2200, USA*

Abstract

As an emerging structural material, high-entropy alloys (HEAs) have significant application potential in high-strain-rate environments and across a range of temperatures, including both high and low temperatures. Previous studies mainly focused on the mechanical behavior of HEAs under high-speed loading or low temperature, which is limited to a single extreme environment. This paper primarily discusses the mechanical behavior and microscopic mechanism of the

---

[1] Corresponding authors. E-mail: qiaojunwei@gamil.com (J. Qiao)

$Fe_{40}Mn_{20}Cr_{20}Ni_{20}$ high-entropy alloy (HEA) at high and low temperatures and high strain rates (Split Hopkinson bar) and utilizes relevant theoretical models to fit the yield strength and flow stress of the HEA. The tensile test results show that the HEA exhibits excellent strength-plastic synergy and excellent work-hardening ability under the condition of reducing temperature or increasing strain rates. During the dynamic tensile process, the interaction of different forms of dislocations and deformation twins together improves the strength and work-hardening ability of the HEA. The Zerilli-Armstrong (Z-A) constitutive model was used to predict the temperature sensitivity and strain-rate sensitivity of the yield strength of the HEA. At the same time, the Taylor model was used to predict the change of the HEA flow stress with the strain rate under dynamic tension, and the model was applied to low-temperature dynamics. The fitting results were consistent with the experimental results, which provided a theoretical basis for the subsequent prediction of HEAs strengths.

***Keywords*:** High-entropy alloy; Dynamic tension; Low temperature; Deformation mechanism; Work hardening

1. Introduction

High-entropy alloys (HEAs) are a unique class of alloys with a high mixing entropy and near-equimolar ratio. They were first proposed by Cantor and Yeh et al. in 2004~~ and have been extensively studied in recent years~~ [1–3]. Its high configuration entropy and topologically ordered lattice structure give HEAs many excellent properties, including an excellent combination of strength and ductility, excellent low-temperature plasticity, excellent corrosion resistance, and wear resistance [4–8]. These properties indicate that HEAs have great application potential in high strain rates and at high or low temperatures. With the development of the aerospace, nuclear, and defense industries, greater requirements have been placed on the performance of materials in extreme environments [9]. Exploring materials with a good balance of strength and plasticity in extreme environments has attracted widespread attention [10,11].

Face-centered-cubic (FCC) HEAs have excellent deformability, and their most prominent mechanical properties are low strength but good plasticity [3]. For example, the CoCrFeMnNi HEA (Cantor alloy) has a good combination of strength and plasticity [1]. Researchers have developed several related alloys based on Cantor alloy. For example, the mechanical properties of CoCrNi [12–14], FeMnCoCr [15,16], and CoCrFeNi HEAs[17–19] ~~in a wide temperature ranges have been widely studied~~. For example, Gali et al. [19] investigated the tensile behavior of CoCrFeNiMn and CoCrFeNi HEAs in the temperature range of 77 K to 1,273 K and the strain rate range of 10^{-3} s^{-1} and 10^{-1} s^{-1}. It was found that the strength and plasticity of the alloys increased simultaneously with the decrease in temperature, which may be due to the nano-scale twins caused by deformation, which delayed the occurrence of necking and further increased the plasticity. At the same time, the appearance of twins makes the alloy have continuous and stable work hardening [20]. Subsequently, considering that the price of the Co element is relatively expensive, some Co-free FeCrNi [21,22] and FeMnCrNi [23] HEAs are gradually derived. These alloys still maintain excellent work-hardening ability and a good combination of strength and plasticity at low temperature or high strain rates.

However, the service environment of most metals and alloys is not under quasi-static conditions, but under high-speed dynamic loads~~, such as aerospace, automotive industry, etc~~. To further explore the application of HEAs under extreme conditions, the study of dynamic deformation behavior is very important. In general, FCC HEAs are more likely to activate deformation twins (DT) under high strain-rate loading~~, resulting in excellent dynamic-mechanical properties~~ [24]. In recent years, researchers have conducted extensive research on the CrMnFeCoNi HEA, including adiabatic shear localization [25], strain-rate sensitivity [26], and impact loading [5]. It has been found that deformation twinning is a common microstructure mechanism of this HEA under extreme loading conditions (such as low temperature or high speed loading) [27,28]. In addition, the CoCrFeNi HEA with a single phase FCC structure is mainly deformed by dislocation slip under quasi-static tension, while deformation twins are easily activated under high-speed dynamic loading [29]. Previous studies on the mechanical properties of the $Fe_{40}Mn_{20}Cr_{20}Ni_{20}$ HEA under dynamic loading showed that the mechanical properties of HEAs were improved due to the activation of deformation twins [30]. Therefore, different deformation mechanisms determine various mechanical responses.

The deformation mechanism of HEAs depends not only on the intrinsic parameters of the material, such as stacking fault energy (SFE), but also on the deformation conditions (such as temperature and strain rate) [31–33].

In this study, a face-centered-cubic (FCC) $Fe_{40}Mn_{20}Cr_{20}Ni_{20}$ high-entropy alloy with a weight of about 500 kg was prepared by industrial vacuum induction melting. Our early work has preliminarily understood the effect of heat treatment on the microstructures and properties of the HEA [30,34]. Therefore, our current research focuses on the microstructure evolution of the alloy under different strain rates and uses relevant theoretical models to analyze and fit its strength and stress, providing a theoretical basis for subsequent alloy strength predictions. Under the condition of reducing temperature or increasing strain rate, the alloy has excellent strength-plastic synergy and excellent work-hardening ability. At 77 K and a 10^{-3} s^{-1} strain rate, the yield strength and ultimate tensile strength of the alloy are 405 MPa and 900 MPa, which are increased by about 78% and 83%, respectively, and the plasticity is as high as 97.5%. With the increase in strain rates, the yield strength of the HEA can reach up to 481 MPa, and the plasticity is still as high as 95%. Compared with the quasi-static tensile experiment, the yield strength of the HEA is 447 MPa at room temperature, and the strain rate of 1,000 s^{-1}, which is increased by about 97%, and the elongation is maintained at a high level. With the increase in the strain rate, there is no contradiction between the strength and plasticity inversion. At low temperatures, the yield strength of the alloy is up to 1,120 MPa, and the plasticity is 45.7%. During the dynamic tensile process, the interaction of different forms of dislocations and deformation twins together improve the strength and work-hardening ability of the $Fe_{40}Mn_{20}Cr_{20}Ni_{20}$ HEA. Finally, the temperature sensitivity and strain-rate sensitivity of the yield strength of the alloy were predicted using the Z-A constitutive model. At the same time, the Taylor model was employed to predict the flow stress change of the alloy under dynamic tension, and the model was applied to the low-temperature dynamic loading, and the fitting results were consistent with the experimental results. Therefore, the excellent mechanical properties of the $Fe_{40}Mn_{20}Cr_{20}Ni_{20}$ HEA under dynamic loading are expected to become a candidate material for impacts-resistant structural materials.

2. Experimental methods

2.1 Alloy preparation

Under industrial production conditions, $Fe_{40}Mn_{20}Cr_{20}Ni_{20}$ high-entropy alloy ingots with a nominal composition of the $Fe_{40}Mn_{20}Cr_{20}Ni_{20}$ were prepared by vacuum induction-melting equipment using pure metal iron, manganese, chromium, and nickel (the purity of each element exceeds 99.95 wt.%). The total weight is about 500 kg. The ingot was homogenized at 1,200 °C for 1.5 h, cooled to room temperature in air, and finally hot rolled into a plate with a thickness of 20 mm.

2.2 Mechanical tensile tests

The quasi-static uniaxial tensile test was conducted using an Instron 5969 tensile tester at different temperatures and strain rates. The dog-bone tensile specimen size was 14 mm × 3 mm × 1 mm, the test temperatures were 77 K – 1,073 K, and the strain rates were 10^{-3} s^{-1} – 10^{-1} s^{-1}. To study the evolution of microstructure with the increase of strain rate, the Split Hopkinson tensile bar (SHTB) was used for dynamic-tensile tests.

The size of the tensile specimen was 10 mm × 4 mm × 1 mm, the test temperatures were 77 K and 298 K, and the strain rate was 1,000 s^{-1}, 1,600 s^{-1} and 2,000 s^{-1}. According to the one-dimensional stress-wave theory, the strain rate, strain, and stress under dynamic tension can be calculated by Eqs. (1) – (3):

$$\dot{\varepsilon}=\frac{\mathrm{d}\varepsilon}{dt}=-\frac{2C_b\varepsilon_r}{L_s} \tag{1}$$

$$\varepsilon=-\frac{2C_b}{L_s}\int_0^t \varepsilon_r(t)dt \tag{2}$$

$$\sigma=\frac{EA_b}{A_s}\varepsilon_t(t) \tag{3}$$

where ε_r and ε_t are the strain signals on the incident rod and the transmission rod, respectively, C_b is the longitudinal wave velocity in the tensile rod, L_s is the cross-sectional length of the sample, A_b is the cross-sectional area of the sample, A_s is the cross-sectional area of the incident rod and the transmission rod, and E is the elastic modulus of the incident rod and the transmission rod. The tensile rod is made of a maraging steel with a yield strength of 1.8 GPa. The rod must be in the elastic stage during the whole loading process. To ensure the reliability of the data, at least three tensile tests were repeated under each condition.

2.3 Microstructural characterization

The initial microstructure of the sample was observed by the Leica DM 6000 metallographic microscope. The phase identification was performed by an X-ray diffractometer (XRD, PANalytical AERIS) with Co *K*α radiation. The grain size of the initial sample was roughly estimated by Image-Pro Plus software. ~~The sheet for the TEM observation was extracted from the center of the cross section of the tensile specimen, and it was mechanically ground to about 30 μm along the thickness direction.~~

The sheet for TEM observation was extracted from about 1 mm below the center of the fracture section of the tensile specimen. The sheet size was about 5 × 5 × 1 mm, and it was mechanically ground to about 30 μm along the thickness direction. Electrochemical thinning was performed using a double-jet polishing instrument at - 10 °C and a 15 V-operating voltage. The selected etchant was a mixed solution (volume ratio) of perchloric acid (10%) and ethanol (90%). Field emission scanning transmission electron microscopy (STEM, FEI Talos F200X G2) and high-resolution transmission electron microscopy (HRTEM) were used to characterize the samples after dynamic stretching.

3. Results

3.1. Initial microstructure

Fig. 1(a) is the XRD pattern and metallographic structure of the hot-rolled HEA. The XRD patterns show that the HEA is a single-phase FCC solid solution structure. The illustration indicates the corresponding metallographic diagram, exhibiting typical equiaxed grains and a small number of annealing twins (ATs) inside the grains. The grain size of the HEA was calculated by the Image-Pro Plus to be about 21.8 μm. Fig. 1(b) is the XRD pattern of the $Fe_{40}Mn_{20}Cr_{20}Ni_{20}$ HEA alloy after stretching at different strain rates at low temperature, which still shows a single-phase FCC structure, indicating that the HEA does not undergo a phase structure transformation after stretching at different strain rates at low temperatures.

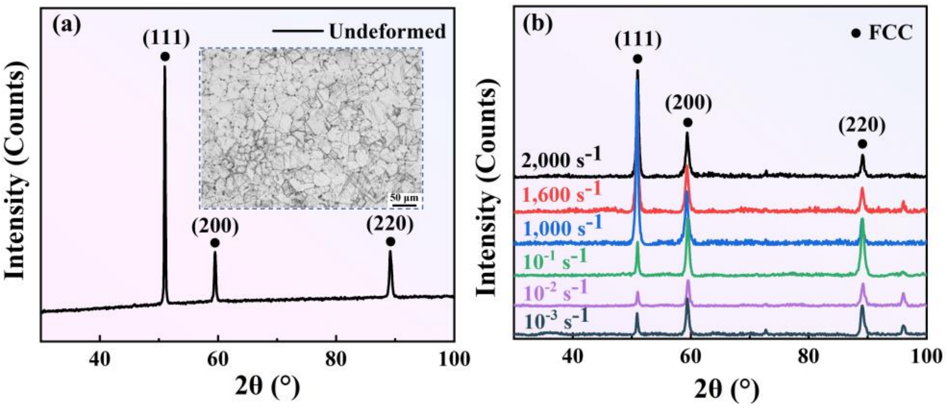

Fig. 1 XRD pattern of the $Fe_{40}Mn_{20}Cr_{20}Ni_{20}$ HEA under different conditions, and the illustration is the metallographic diagram of the hot-rolled HEA. (a) Hot-rolled HEA; (b) The alloy after stretching at different strain rates at low temperatures

3.2 Tensile performance at different temperatures

Fig. 2 shows the engineering stress-strain curves of the $Fe_{40}Mn_{20}Cr_{20}Ni_{20}$ HEA at different temperatures (298 K, 473 K, 673 K, 873 K, and 1,073 K), revealing the changes in strength and plasticity of the alloy with temperature. At the same time, Table 1 shows the specific values of strength and plasticity of the alloy at different temperatures. At room temperature, the yield strength (YS) and ultimate tensile strength (UTS) of the HEA are 227 MPa and 491 MPa, respectively, and the uniform elongation is 43.4%. This is similar to most FCC structure HEAs [11,29], showing a good combination of strength and plasticity. It can be seen from the Fig. 2 that as the test temperature increases, the alloy softens, which is similar to the situation of most alloys at high temperatures [35–37]. ~~When the temperature is 473 K, the strength and plasticity of the alloy are not significantly reduced; When the temperature is 1,073 K, the yield strength of the alloy is less than 100 MPa, the ultimate tensile strength is only 123 MPa, the uniform elongation is also reduced to 17.5%, and the softening phenomenon is significant.~~ When the temperature is 1073 K, the alloy appears obvious softening phenomenon.

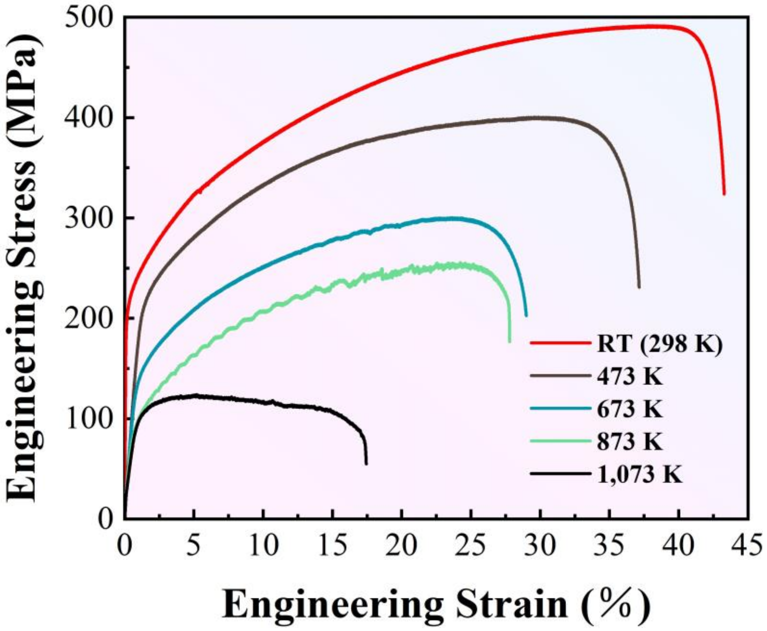

Fig. 2 The engineering stress-strain curve of the $Fe_{40}Mn_{20}Cr_{20}Ni_{20}$ HEA at 298 K – 1,073 K under a quasi-static condition

Table 1 The strength and plasticity data of the $Fe_{40}Mn_{20}Cr_{20}Ni_{20}$ HEA at 298 K – 1,073 K under a quasi-static condition

T (K)	Yield strength (MPa)	Ultimate tensile strength (MPa)	Uniform elongation (%)
298	227	491	43.4
473	207	400	37.2
673	135	301	29.2
873	101	253	27.8
1,073	95	123	17.5

Fig. 3 is the engineering stress-strain curve of the $Fe_{40}Mn_{20}Cr_{20}Ni_{20}$ HEA under low temperature quasi-static (0.001 s^{-1},0.01 s^{-1} and 0.1 s^{-1}) conditions. In Table 2, the specific values of strength and plasticity of current HEA at different strain rates under low temperature quasi-static conditions are given. Compared with the quasi-static state at room temperature, the strength and plasticity of the alloy at low temperature were significantly improved. ~~When the strain rate was 0.001 s^{-1}, the yield strength and ultimate tensile strength of the alloy were 405 MPa and 900 MPa, and the uniform elongation was as high as 97.5%. Both the strength and plasticity were doubled. With the increase in the strain rate, the yield strength and ultimate tensile strength of the alloy increase to 481 MPa and 912 MPa, and the uniform elongation can still reach 95.0%.~~ HEAs with FCC structures have the characteristics of high strength and high plasticity at low temperatures [38,39]. The illustration was the fracture diagram of the alloy after 0.001 s^{-1} stretching, showing a large number of dimples, and the dimples were small, indicating that the alloy had undergone high plastic deformation during the stretching process. ~~At the same time, the gauge length of the tensile specimen after the tests is about 19.5 mm, which is consistent with the experimental results.~~

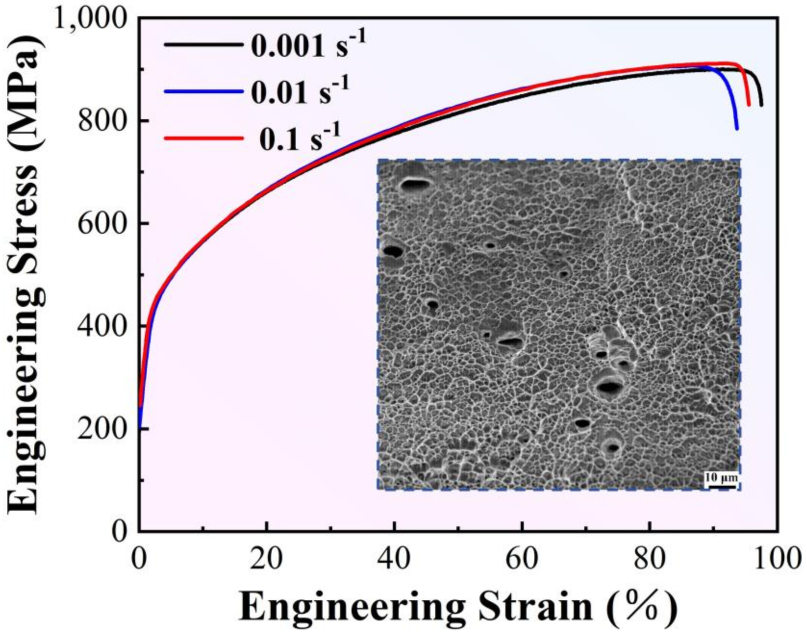

Fig. 3 Tensile curves of the $Fe_{40}Mn_{20}Cr_{20}Ni_{20}$ HEA at different strain rates at low temperature (77 K), illustrated with a 0.001 s^{-1} port diagram

Table 2 Strength and plasticity of the $Fe_{40}Mn_{20}Cr_{20}Ni_{20}$ HEA at different strain rates at a low temperature (77 K)

$\dot{\varepsilon}$ (s^{-1})	Yield strength (MPa)	Ultimate tensile strength (MPa)	Uniform elongation (%)
10^{-3}	405	900	97.5
10^{-2}	418	907	93.6
10^{-1}	481	912	95.0

3.3 Mechanical properties under dynamic tension at room temperature and low temperature

Fig. 4 is the engineering stress-strain curve and true stress-strain curve of the $Fe_{40}Mn_{20}Cr_{20}Ni_{20}$ HEA under room temperature dynamic loading (1,000 s^{-1}, 1,600 s^{-1}, and 2,000 s^{-1}), and the specific location of the yield strength ($\sigma_{0.2}$) point was given in the Fig. 4. The work-hardening behavior with the increase of strain rates under different deformation conditions and the excellent combination of strength and plasticity under dynamic loads were revealed. Compared with the quasi-static state, the dynamic tension showed a typical strength-plasticity inversion phenomenon [11]. When the strain rate was 1,000 s^{-1}, the yield strength and ultimate tensile strength of the alloy increased by about twice, ~~from 227 MPa and 491 MPa to 447 MPa and 1,198 MPa, respectively,~~ and maintained a high elongation of 25.3%. At the same time, obvious secondary work-hardening behavior occurs at 1,000 s^{-1}, resulting in a higher ultimate strength of the alloy. The promotion of secondary work hardening at high strain rates leads to the complexity of work-hardening behavior during the dynamic tensile process. When the strain rate was 2,000 s^{-1}, the yield strength and plasticity of the alloy increased significantly~~, which were about 995 MPa and 44.5%, respectively~~. Plasticity is comparable to that of the quasi-static alloy, but the strength increases significantly. As Qiao et al. [29] put forward the rule of “the higher the speed, the stronger the toughness” for the FCC-structured HEA.

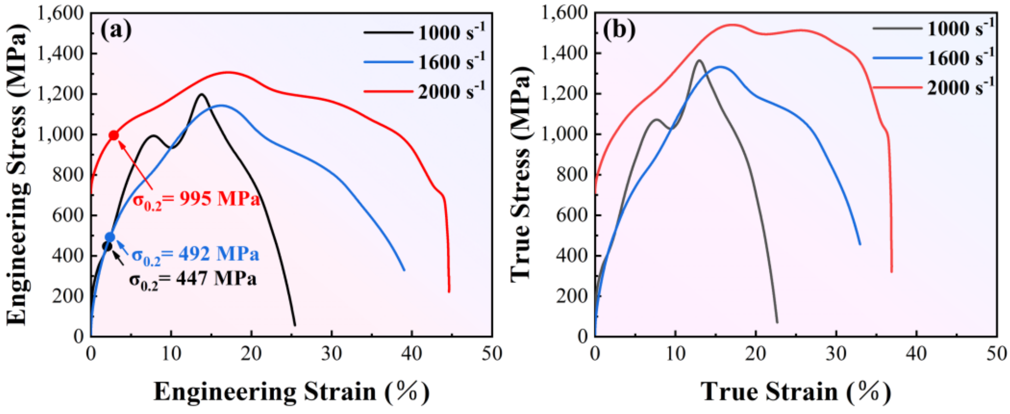

Fig. 4 The tensile curves of $Fe_{40}Mn_{20}Cr_{20}Ni_{20}$ HEA at different strain rates at room temperature.

(a) Engineering stress-strain curve; (b) True stress-strain curve

Fig. 5 shows the engineering stress-strain curve and true stress-strain curve of $Fe_{40}Mn_{20}Cr_{20}Ni_{20}$ HEA under low temperature dynamic loading (1,000 s^{-1}, 1,600 s^{-1}, and 2,000 s^{-1}), and the specific location of yield strength ($\sigma_{0.2}$) point was given in the Fig. 5. Compared with the room temperature dynamic, the yield strength of the alloy at low temperature (77 K) dynamic loading was obviously improved, and the ultimate tensile strength was slightly increased, and the elongation was basically unchanged. ~~When the strain rate was 2,000 s^{-1}, the yield strength and ultimate tensile strength of the alloy were 1,120 MPa and 1,660 MPa, respectively, and the plasticity was as high as 45.7%.~~ At the same time, compared with the quasi-static state at low temperature, the strength of the $Fe_{40}Mn_{20}Cr_{20}Ni_{20}$ HEA at low temperature increased by about one time, but the plasticity decreased in the same proportion, and the phenomenon of the strength-plasticity inversion also appeared. Finally, the specific values of strength and plasticity of the alloy under dynamic tension at room temperature (298 K) and low temperature (77 K) were listed in Table 3. The length of the gauge section of the tensile specimen after the test was basically consistent with the uniform elongation obtained by the experimental results.

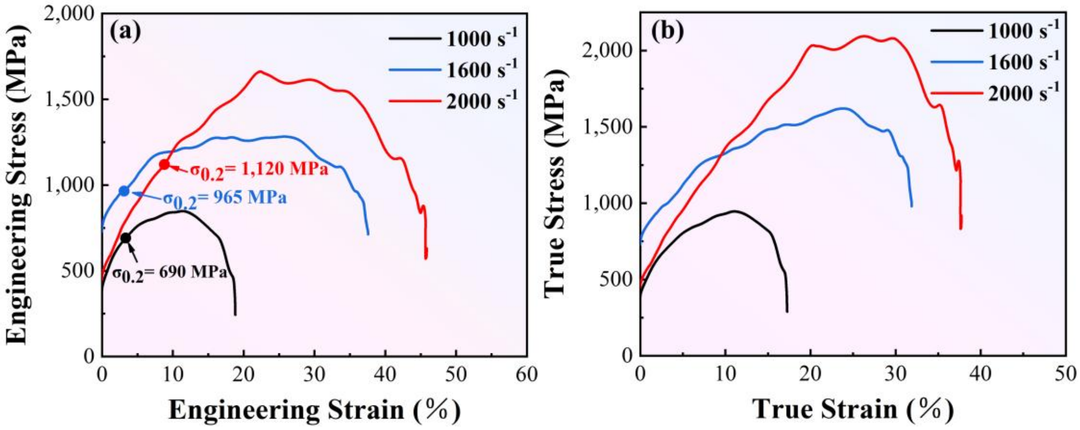

Fig. 5 The tensile curves of the $Fe_{40}Mn_{20}Cr_{20}Ni_{20}$ HEA at different strain rates at low temperature (77 K). (a) Engineering stress-strain curve; (b) True stress-strain curve

Table 3 Strength and plasticity of the $Fe_{40}Mn_{20}Cr_{20}Ni_{20}$ HEA at different strain rates at room temperature (298 K) and low temperature (77 K)

T (K)	$\dot{\varepsilon}$ (s^{-1})	Yield strength (MPa)	Ultimate tensile strength (MPa)	Uniform elongation (%)
298	1,000	447	1,198	25.3
	1,600	492	1,143	39.0
	2,000	995	1,307	44.5
77	1,000	690	848	18.8
	1,600	965	1,275	37.5
	2,000	1,120	1,660	45.7

This study summarizes the yield strength of various metals and alloys under dynamic deformation at room temperature and low temperature, and the strain rate was mainly 10^3 s^{-1}. As shown in Fig. 6, the yield strength of the $Fe_{40}Mn_{20}Cr_{20}Ni_{20}$ HEA was in the middle and upper positions of the figure at similar strain rates. Compared with titanium alloy, the alloy shows a lower yield strength. However, compared with magnesium alloy and aluminum alloy, the yield strength of the HEA was significantly improved. At low temperature dynamic loading, the current alloy exhibits a yield strength very close to that of the CoCrFeMnNi HEA. Therefore, the $Fe_{40}Mn_{20}Cr_{20}Ni_{20}$ HEA exhibits excellent dynamic-mechanical properties compared to most metal materials, and is expected to become a candidate material for super-strength structural materials.

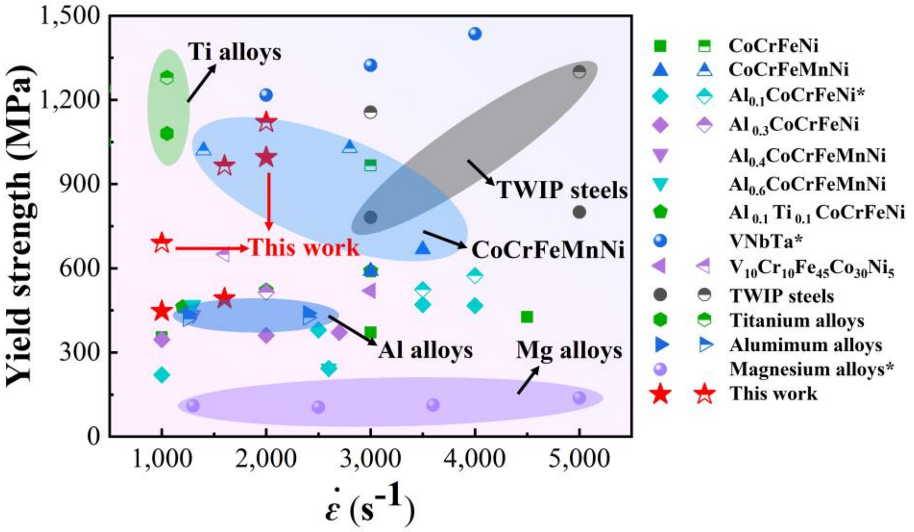

Fig. 6 Comparison of mechanical properties of common metals, alloys, and some high-entropy alloys under dynamic deformation. * represents dynamic-compression deformation

3.4 Microstructure after dynamic tensile loading

3.4.1 EBSD characterization after dynamic tensile

As shown in Figs. 7 and 8, the microstructure of the $Fe_{40}Mn_{20}Cr_{20}Ni_{20}$ HEA after dynamic tensile loading was characterized by EBSD, and the changes of the recrystallization fraction, grain-boundary type, and dislocation density of the HEA after deformation were analyzed. As shown in Fig. 7, the grain morphology, deformation degree, and volume fractions of different types of grain boundaries (LAGBs, HAGBs, and Σ3 twin boundaries) and KAM value of the alloy changed significantly after dynamic tensile loading at room temperature, indicating that the HEA had obvious plastic deformation [40]~~. When the strain rate is 1,000 s^{-1}, the deformed grains in the alloy reach 83.3%. The corresponding KAM diagram shows that only a small number of grains participate in plastic deformation~~. With the increase of strain rates, the proportion of deformed grains, LAGBs and KAM values in the HEA increase significantly, while the proportion of HAGBs and Σ3 twin boundaries decreases. The corresponding illustrations use specific data to describe the deformation degree of the HEA more accurately.

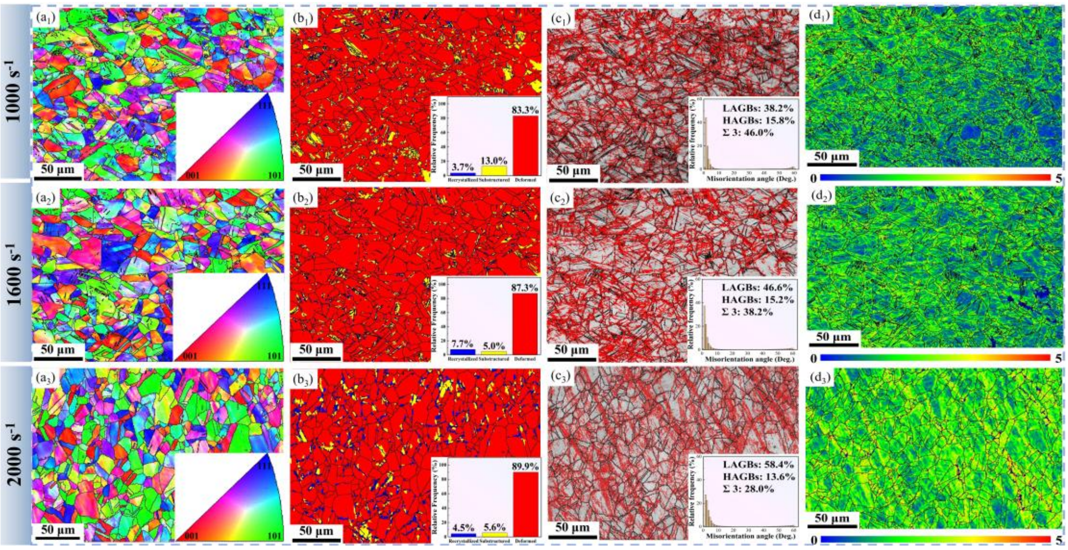

Fig. 7 EBSD diagram of the alloy at different strain rates after dynamic tensile loading at room temperature. (a) IPF diagram; (b) Recrystallization-distribution map and illustrations of statistical results of recrystallization fractions; (c) Large and small angle grain-boundary diagram; (d) KAM diagram

As shown in Fig. 8, the alloy generated more severe plastic deformation after low temperature dynamic tensile loading. At the same strain rate, the alloy after low temperature dynamic tensile loading shows a higher proportion of deformed grains, a smaller proportion of high-angle grain boundaries and a higher KAM value. At the same time, the proportion of Σ3 twin boundaries is greater, indicating an increase in the number of deformation twins [34]. With the increase of strain rates, the change of grain structures in the alloy is similar to that at room temperature, which is manifested as the increase of the proportion of deformed grains, small-angle grain boundaries, and KAM value, and the decrease of the proportion of large-angle grain boundaries. The corresponding KAM diagram shows that the KAM values are higher under low temperature dynamic tensile loading, and this highly deformed region appears not only on the grain boundary, but also inside the grain. It is shown that almost all grains in the alloy are involved in plastic deformation after low temperature dynamic tensile loading.

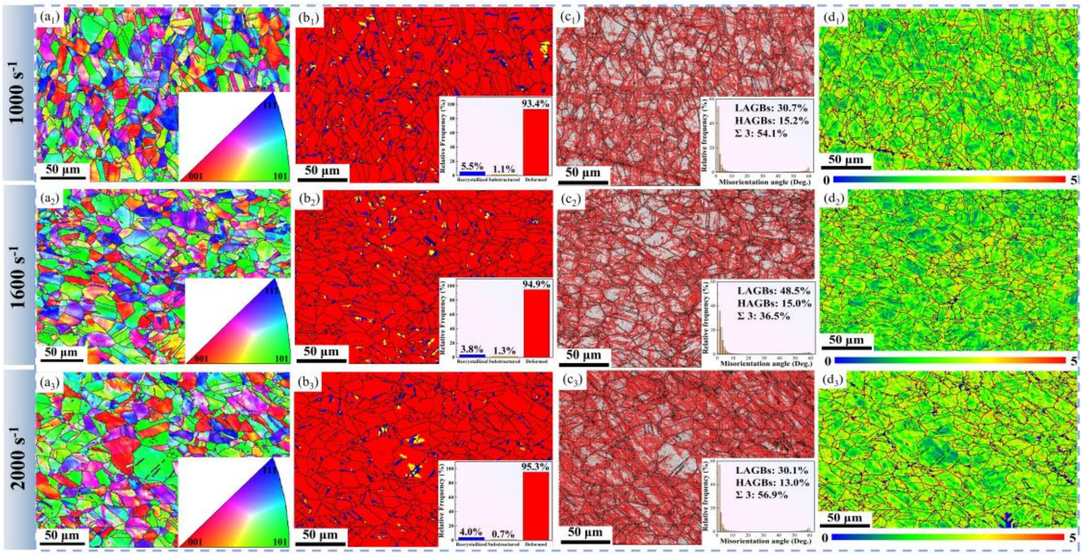

Fig. 8 EBSD diagram of the alloy at different strain rates after dynamic tensile loading at low temperature. (a) IPF diagram; (b) Recrystallization-distribution map and illustrations of statistical results of recrystallization fractions; (c) Large and small angle grain-boundary diagram; (d) KAM diagram

3.4.2 Dislocation configuration after dynamic tensile

Figs. 9 and 10 present the TEM images of the $Fe_{40}Mn_{20}Cr_{20}Ni_{20}$ HEA related to dislocation structures after dynamic tension at strain rates of 1,000 s^{-1}, 1,600 s^{-1}, and 2,000 s^{-1} at room temperature, showing different forms of dislocation structures, such as dislocation lines, dislocation cells, dislocation tangles, and dislocation walls. At the strain rate of 1,000 s^{-1}, the plastic deformation was still dominated by dislocation slips~~, and the dislocation density was relatively low~~. With the increase in the strain rate, the overall dislocation density increases. ~~High-density dislocations aggregate into dislocation cells, which refine grains and form nano-grains.~~ In addition, the smaller dislocation cells in the tensile specimen provided a higher flow stress for the alloy [41]. At the same time, ~~high-density dislocation lines were entangled with each other in the~~

~~dislocation wall, while the intracellular dislocation density was relatively low, and~~ t The dislocation structure changed from the planar slip to wavy slip (i.e., dislocation cell structure). It is reported that this slip-transition phenomenon also occurs in $Fe_{40}Mn_{40}Co_{10}Cr_{10}$ and NiCoCrFeMn HEAs [39,42].

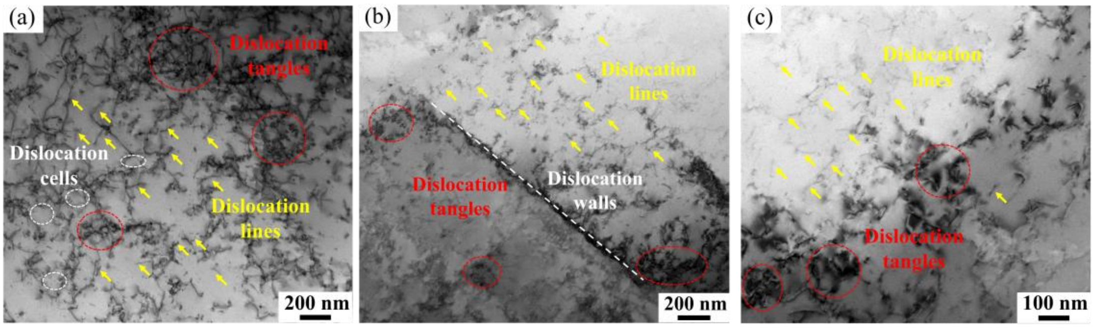

Fig. 9 The dislocation structures of the $Fe_{40}Mn_{20}Cr_{20}Ni_{20}$ HEA with different morphologies at room temperature and 1,000 s^{-1} strain rate. Including dislocation cells (white circle), dislocation lines (yellow arrow), dislocation walls (white dotted line) and dislocation tangles (red circle)

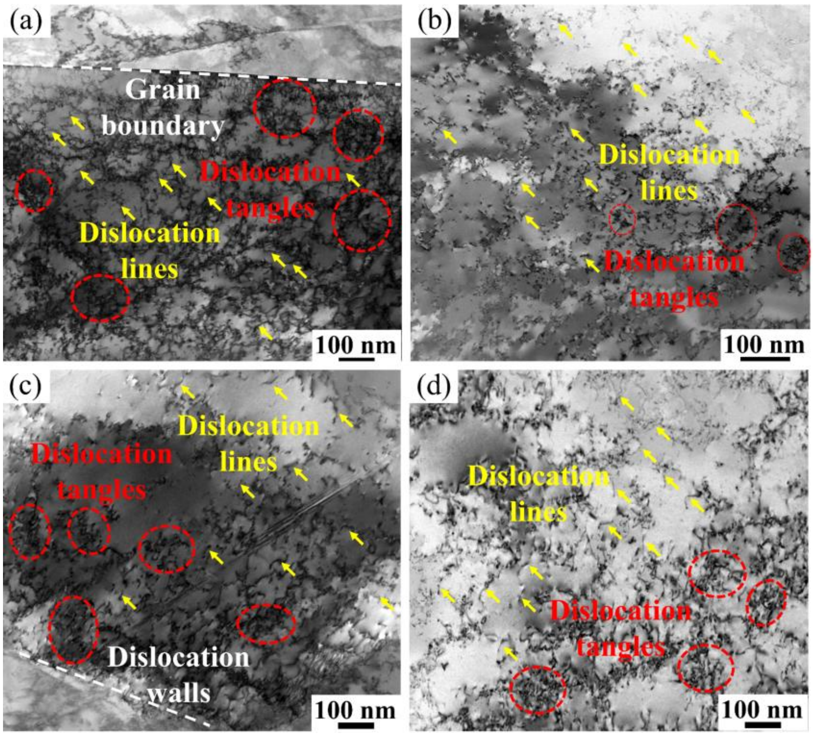

Fig. 10 The dislocation structure of the $Fe_{40}Mn_{20}Cr_{20}Ni_{20}$ HEA with different morphologies at room temperature and different strain rates. (a) and (b) 1,600 s^{-1}; (c) and (d) 2,000 s^{-1}. Including dislocation lines (yellow arrow), dislocation walls (white dotted line) and dislocation tangles (red circle)

Fig. 11 shows the TEM images related to the dislocation structure of the $Fe_{40}Mn_{20}Cr_{20}Ni_{20}$ HEA after dynamic tension at low temperature (77 K) and strain rates of 1,000 s^{-1}, 1,600 s^{-1}, and 2,000 s^{-1}. At low temperature, the dislocation density increased obviously with the increase of strain rates. Compared with the dynamic state at room temperature, the dislocation density at low temperature was also significantly increased. The interaction between dislocations and grain boundaries resulted in high-density dislocation tangles, which is the result of dislocation cross-slip [30]. At the same time, the appearance of high-density dislocation walls (HDDWs) (As shown in Fig. 10c) indicated that the dislocation motion changes from planar slip to cross slip or multiple slip after high strain rate deformation. The high-density dislocation walls in HEAs will affect the slip of isolated dislocations, activate the accumulation, absorption, or transfer of dislocations, and its movement will lead to the release of local stress, enhance the work-hardening ability of HEAs, and improve its strength and plasticity [43]. Therefore, high-density dislocations become one of the factors that increase the flow stress of the HEA under dynamic loading.

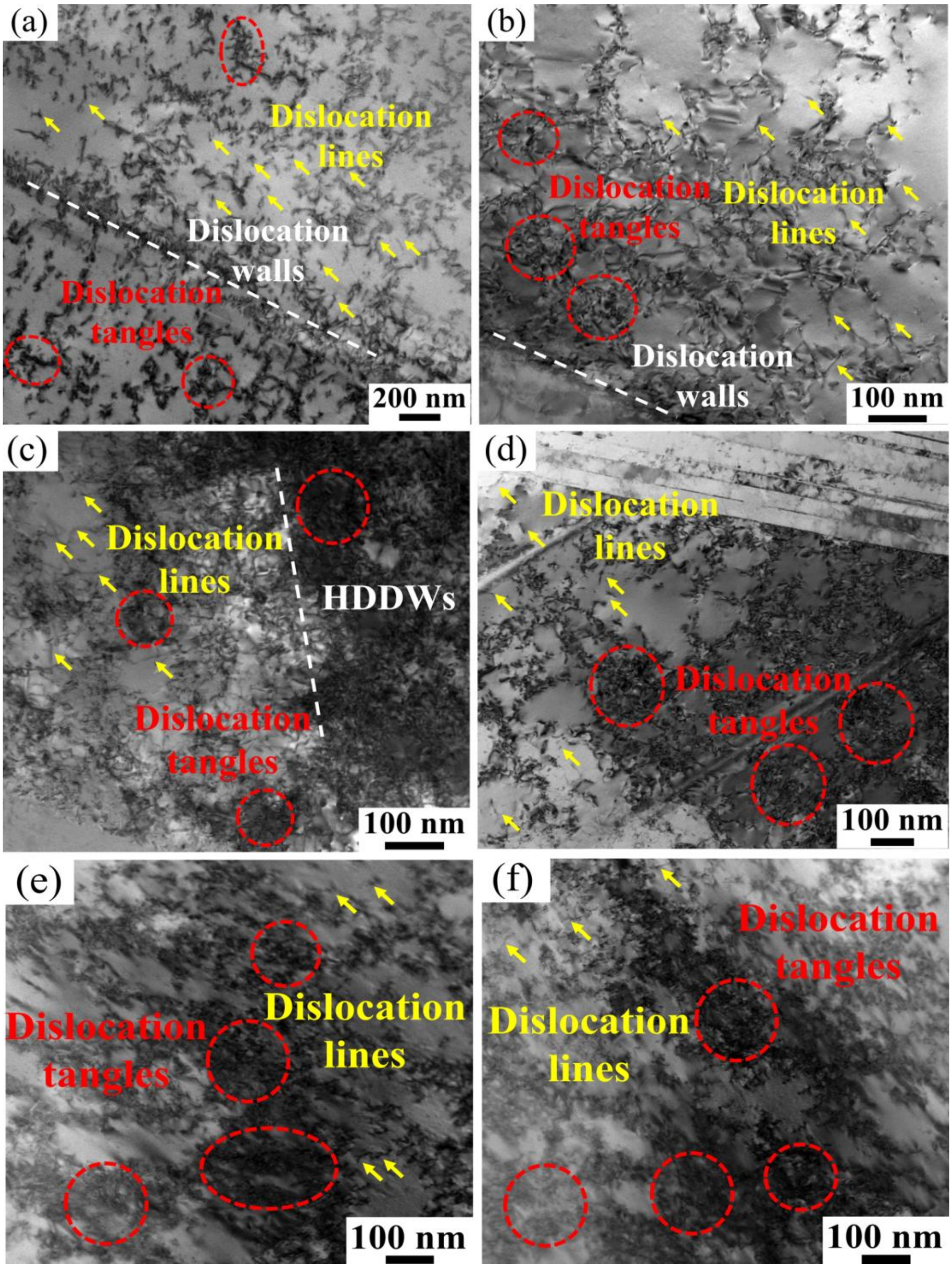

Fig. 11 The dislocation structures of the $Fe_{40}Mn_{20}Cr_{20}Ni_{20}$ HEA at different strain rates at low temperature (77 K). (a) and (b) 1,000 s^{-1}; (c) and (d) 1,600 s^{-1}; (e) and (f) 2,000 s^{-1}. Including dislocation lines (yellow arrow), dislocation walls and high-density dislocation wall (white dotted line) and dislocation tangles (red circle)

3.4.1 Twins configuration after dynamic tensile loading

At room temperature, the $Fe_{40}Mn_{20}Cr_{20}Ni_{20}$ HEA exhibited a deformation twins structure after dynamic tension at strain rates of 1,600 s^{-1} and 2,000 s^{-1}, as shown in the yellow dotted line in Fig. 12. After dynamic tension, nano-scale deformation twins along the [011] crankshaft appear, and the corresponding selected area electron diffraction pattern shows diffraction spots belonging to the FCC twins and matrix. As the strain rate increases, the number of twins increases, and the twin width decreases from 31.2 nm to 19.5 nm. ~~The high-resolution diagram of twins confirmed the coherent relationship between twin boundaries and the matrix.~~ Deformation twins are usually observed after severe plastic deformation in medium/low SFE alloys, which is an important deformation mechanism to increase the work-hardening ability and mechanical properties of HEA [44].

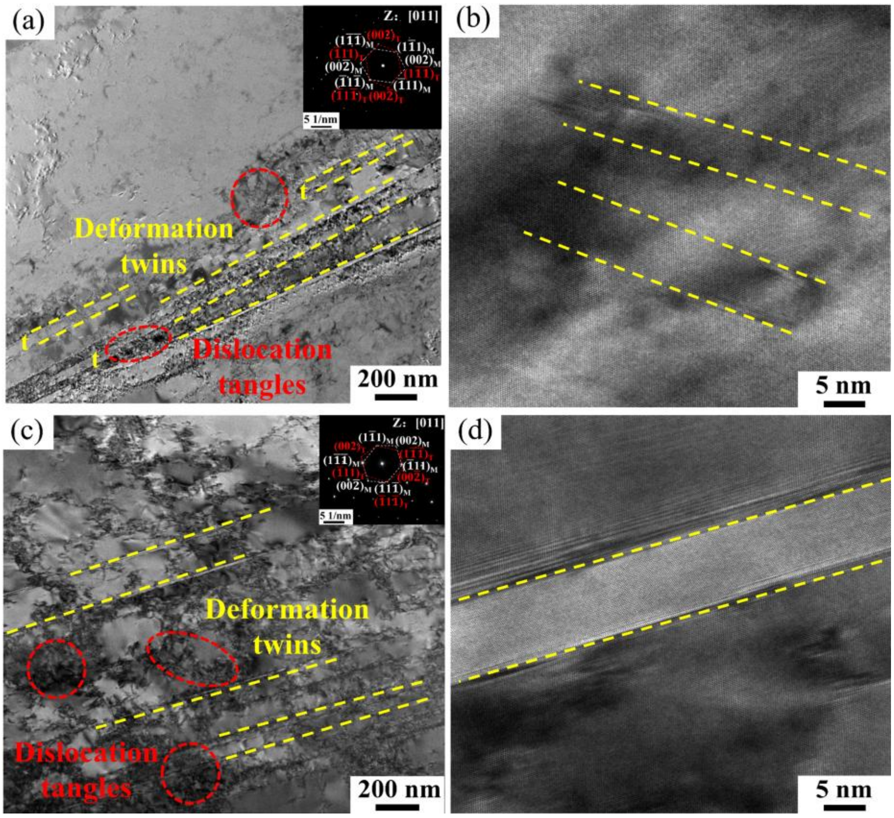

Fig. 12 The twin structure of the $Fe_{40}Mn_{20}Cr_{20}Ni_{20}$ HEA at room temperature and different strain rates. (a) and (b) 1,600 s^{-1}; (c) and (d) 2,000 s^{-1}.The yellow dotted line represents the deformation twins, *t* is the twin width, and the red circle represents the partial dislocation structure

As shown in Fig. 13, a large number of close-packed deformation twins also appear in the $Fe_{40}Mn_{20}Cr_{20}Ni_{20}$ HEA after dynamic tension at strain rates of 1,000 s^{-1}, 1,600 s^{-1}, and 2,000 s^{-1} at low temperature. The corresponding selected area electron diffraction pattern shows diffraction spots belonging to the FCC twins and matrix. Compared with room temperature dynamic loading, the number of deformation twins increased significantly under low temperature dynamic loading, and deformation twins appeared in two directions with an angle of about 70°. A large number of dislocations pile-ups appeared at the junction of twins, which inhibited dislocation slips. At the same time, the corresponding high-resolution TEM images show clear twin boundaries. The appearance of nano-twins will destroy the slip trajectory of dislocations and make dislocations concentrate near the twin boundaries, thus indirectly weakening the characteristics of dislocation cells [23]. This process not only improves the strength of the HEA but also improves the plasticity. At low temperature, with the increase of strain rate, the twin width also decreases, which are 32.4 nm, 25.5 nm, and 16.1 nm, respectively. Therefore, deformation twinning is a common microstructure mechanism of the high-entropy alloys under extreme conditions (low temperature and high-speed load).

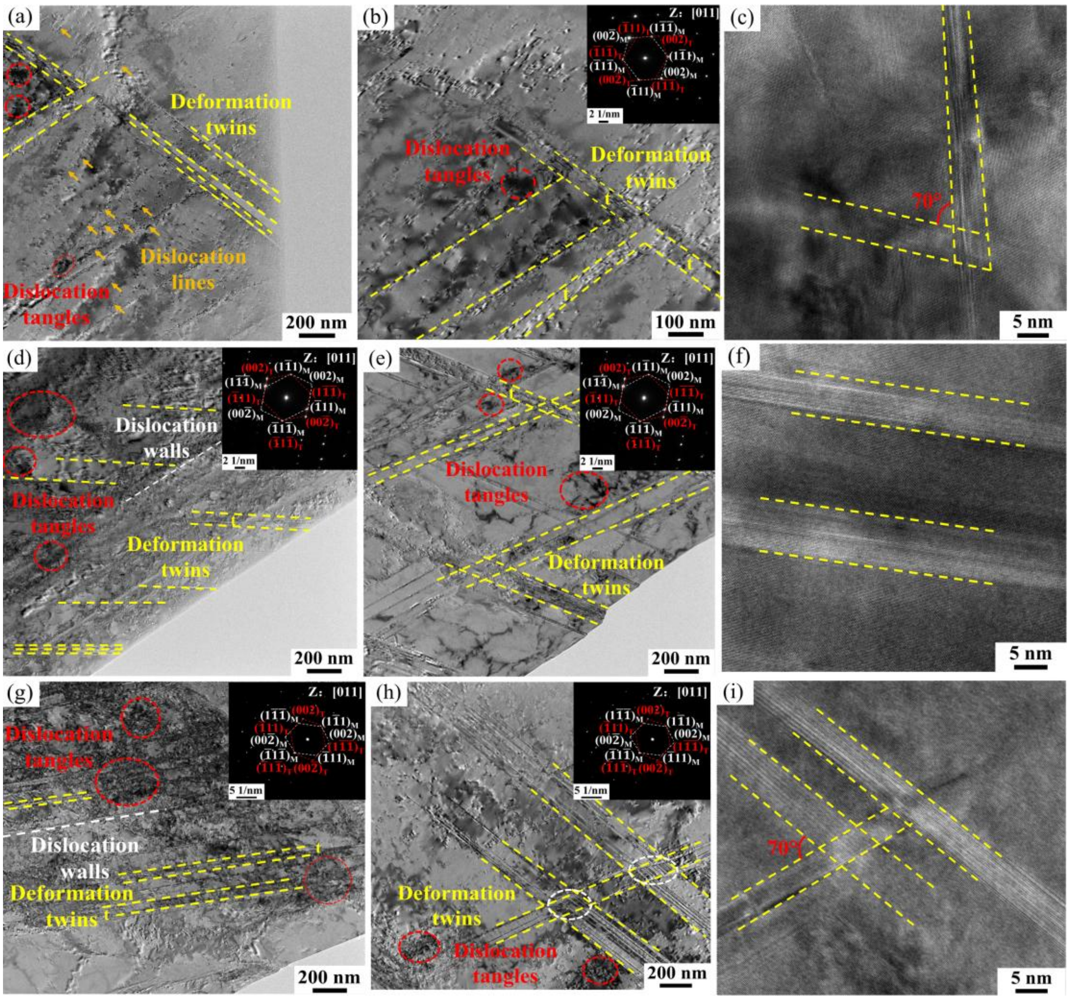

Fig. 13 Twinning structures of the $Fe_{40}Mn_{20}Cr_{20}Ni_{20}$ HEA at different strain rates at low temperature (77 K). (a-c) 1,000 s^{-1}; (d-f) 1,600 s^{-1}; (g-i) 2,000 s^{-1}.The yellow dotted line represents the deformation twins, *t* is the twin width, and the red circle represents the partial dislocation structure

4. Discussions

4.1 Yield-strength model of thermal-activation mechanisms

In the process of plastic deformation, the deformation mechanism can be divided into thermally activated dislocation motion, dislocation drag, and relativistic effect mechanism based on different dislocation velocities [11]. The thermal-activation mechanism is a dislocation-motion mechanism based on the dislocation-motion law and dislocation dynamics. It usually dominates plastic deformation at low strain rates [45]. Dislocation drag, namely phonon drag, refers to the interaction between dislocation and lattice vibration under high strain rate deformation, which affects dislocation motion and strengthens the properties of the HEAs, For example, the dislocation drag effect of CoCrFeNi HEA is significantly improved when the strain rate is greater than 3000 / s[29]. The dislocation drag effect will be discussed in detail later. Relativistic effect is similar to dislocation drag, mainly in extreme conditions (such as high-speed dislocation motion or high-energy particle irradiation) may have an effect on dislocation motion. The mechanism believes that dislocations encounter many obstacles during movement. These obstacles can be divided into short-range thermal obstacles and long-range thermal obstacles[45]. ~~A short-range thermal barrier is sensitive to strain rates and temperatures. A long-range thermal barrier is not sensitive to strain rates and temperatures [45]. Short-range thermal barriers are obstacles that dislocations need to cross when moving, while long-range dislocations without thermal barriers cannot cross, and can only be piled up, bypassed, or sheared.~~ At present, the thermally activated constitutive model used to describe the temperatures and strain rates of materials during deformation is proposed by Zerilli and Armstrong, and the expression is described as follows [46]:

$$\sigma_y = \sigma_0^* \exp(-\beta_0 T + \beta_1 T \ln \dot{\varepsilon}) + \sigma_g \tag{4}$$

where β_0 and β_1 are material constants, T is the absolute temperature, and σ_0^* is the thermal stress at T = 0 K. Since the $Fe_{40}Mn_{20}Cr_{20}Ni_{20}$ HEA is a single-phase FCC structure, and the initial dislocation density is extremely low, only the grain boundary strengthening term, σ_g, is the non-thermal stress in this study.

The Hall-Petch coefficient of the FeMnCrNi HEA has been reported to be (494 MPa·$\sqrt{\mu m}$) [47]. Combined with the related grain size (21.8 μm), the grain-boundary-strengthening term, σ_g, of the FeMnCrNi HEA is calculated to be 106 MPa. The experimental results of wide temperatures and strain rates of the FeMnCrNi HEA are described by the constitutive model of thermal-activation mechanisms. The fitting results were shown in Fig. 14(a). It was found that the thermal-activation mechanism can well reflect the temperatures and strain rates related yield strength of the HEA, and the fitting parameters are self-consistent. The obtained σ_0^*, β_0, and β_1 were 396 MPa, 2.2×10^{-3} / K, and 2.0×10^{-4} / K, respectively. Substituting the parameters into the yield strength constitutive model of the thermal activation mechanism, the predicted yield strengths of the HEA at 77 K, 0.001 s^{-1}, and 1,073 K, 0.001 s^{-1} were 408 MPa and 90 MPa, which were close to the experimental values of 405 MPa and 95 MPa. The above trend is sufficient to illustrate the validity of the yield strength model and can be used for strength predictions.

However, at higher strain rates, The constitutive model of the thermal activation mechanism cannot evaluate the yield strength well, as presented in the blue curve in Fig. 14(b), and the model needs to be modified. Under high strain rate deformation, the interaction between the dislocation and lattice vibration (i.e., phonon viscosity) cannot be ignored, and it affects dislocation motion and plays a strengthening role, which is called phonon traction. Therefore, at high strain rates, phonon drag must be considered in the strain-rate sensitivity of yield strength. By referring to the work of Zerilli and Armstrong [48], the thermally activated strain rate analysis (TASRA) model, including the phonon drag mechanism, is simplified as follows:

$$\sigma_y = \sigma_0^* \exp(-\beta_0 T + \beta_1 T \ln \dot{\varepsilon}) / (1\text{-c}\,\dot{\varepsilon})^{\beta_1 T} + \sigma_g \tag{5}$$

where c is the material constant. The modified model and the previous fitting parameters were used to fit the strength of the alloy after high strain rate stretching. It was found that the phonon traction began to play a role at a strain rate of about 1×10^3 s^{-1} and well reflected the yield-strength sensitivity at high strain rates. The c value was 4.98×10^{-4} s, and the fitting results are shown in the red curve in Fig. 14(b). This trend was similar to the research results of Zhang et al. [29] on the yield-strength sensitivity of the FeCoCrNi HEA at high strain rates.

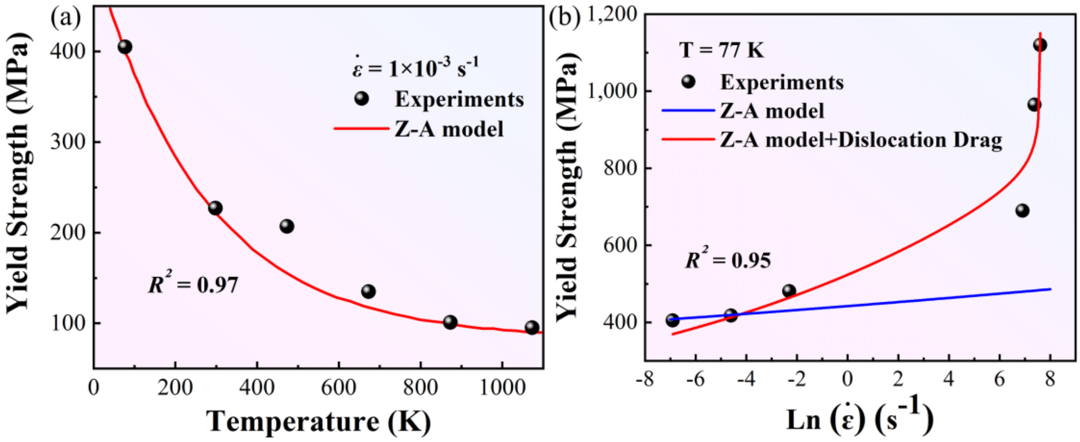

Fig. 14 Experimental data and Z-A model fitting results of the $Fe_{40}Mn_{20}Cr_{20}Ni_{20}$ HEA at low temperature (77 K). (a) Temperature sensitivity of yield strength; (b) Strain-rate sensitivity of yield strength

4.2 Work-hardening constitutive equation related to strain rates

There may be three mechanisms in the dynamic loading process of materials: work hardening, strain-rate hardening, and thermal softening [45]. The former two usually cause an increase of the flow stress, while the thermal softening will reduce the flow stress. In the process of plastic deformation, plastic work is usually converted into heat, resulting in a thermal softening phenomenon. The change of an adiabatic temperature rise with true strain during thermal softening can be calculated by the following equation [45]:

$$\Delta T = T - T_0 = \int_{T_0}^{T} dT = \frac{\beta}{\rho C_P}\int_0^{\varepsilon_P} \sigma d\varepsilon_P \tag{6}$$

where, ΔT is the adiabatic temperature rise, T is the instantaneous temperature of tensile deformation, T_0 is the initial temperature of the test, the value is 298 K or 77 K, β is the fraction of plastic energy converted into heat energy, take 0.9 [49], ρ is the density of the $Fe_{40}Mn_{20}Cr_{20}Ni_{20}$ HEA, about 7.9 g/cm^3, C_p is the constant pressure molar heat capacity, which is estimated by the mixing rule to be 0.454 J/(mol • K) [50], and ε_p is the true strain. The fitting results are shown in Fig. 15. The temperature rises of 1,000 s^{-1}, 1,600 s^{-1}, and 2,000 s^{-1} at room temperature were 68.0 K, 94.5 K and 120.9 K, respectively. The temperature rises of 1,000 s^{-1}, 1,600 s^{-1}, and 2,000 s^{-1} at low temperature (77 K) were 37.7 K, 102.0 K and 157.3 K, respectively. According to the experimental results in this paper, adiabatic shear bands are not observed, and the calculated results show that the adiabatic temperature rise is too small to soften the alloy. Hence, the effect of the adiabatic temperature rise on strain hardening is ignored.

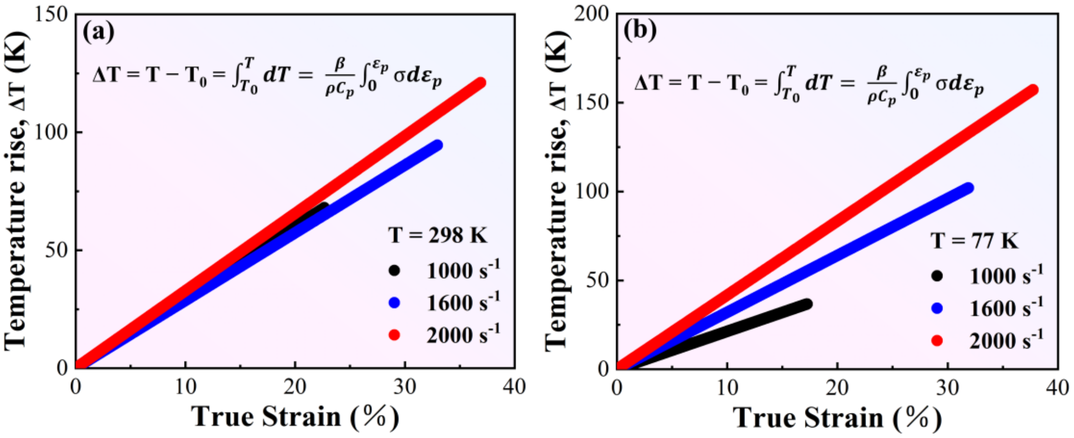

Fig. 15 The temperature rise curves of the Fe$_{40}$Mn$_{20}$Cr$_{20}$Ni$_{20}$ HEA at different temperatures and strain rates. (a) The temperature rise curve at room temperature (298 K); (b) Temperature rise curve at low temperature (77 K)

In this study, microstructure analysis shows that both dislocation strengthening and twinning strengthening contribute to work hardening. Based on the classical Taylor model, a constitutive model based on the micro-deformation structure is developed. The stress induced by forest dislocation is calculated as follows [51]:

$$\sigma_f = M\alpha Gb\sqrt{\rho} \tag{7}$$

where, M is the average Taylor factor, and the FCC metal usually has a value of 3.06.

G is the shear modulus (the shear modulus of the $Fe_{40}Mn_{20}Cr_{20}Ni_{20}$ HEA at 298 K is 85 GPa [23]). α is a constant related to the strength of dislocation interactions, which is 0.4 at room temperature [52]. b is the Burgers vector of the full dislocation. ρ is the total dislocation density. The evolution of dislocation density depends on the dynamic competition of dislocation generation and annihilation. The Kocks-Mecking equation describes the change of dislocation density with strain [53]:

$$\frac{d\rho}{d\varepsilon_p} = M(\frac{1}{b\wedge} - k\rho) \tag{8}$$

where, Λ is the average free path of dislocation, and the corresponding calculation is listed below. k is a dynamic recovery factor related to temperature and strain rate, which is calculated as follows [53]:

$$k = k_0(\frac{\dot{\varepsilon}}{\dot{\varepsilon}_0})^{-\frac{KT}{A}} \tag{9}$$

where, k_0 is the recovery factor at 0 K, which can be calculated by formula (10). K is a Boltzmann constant with a value of 1.38×10^{-23} J/K. $\dot{\varepsilon}_0$ is the reference strain rate, which is 10^7 s^{-1} in this chapter. T is the instantaneous temperature during the deformation process. Because the temperature rise is small, it is considered to be a constant value here (298 K or 77 K). A is a material parameter that depends on the stacking fault energy and can be calculated by equation (11) [54]:

$$k_0 = \exp(\frac{79305\xi^{1.4213}}{1+15001\xi^{1.4213}}) \tag{10}$$

$$\frac{A}{Gb^3} = \frac{1}{\exp(1.44 + 27.55\xi - 390.54\xi^2)} \tag{11}$$

where, ξ is the normalized stacking fault energy, and $\xi = \gamma_{SF}/Gb$. The stacking faults of the $Fe_{40}Mn_{20}Cr_{20}Ni_{20}$ HEA at 298 K and 77 K were 42.6 mJ/m^2 and 14.6 mJ/m^2, respectively [30,34]. Substituting it into the above formula, the values of k_0 at room temperature and low temperature were 36.8 and 4.6, and the values of A were 4.8×10^{-18} J and 5.5×10^{-18} J, respectively.

The microstructure observation before shows that twins play a crucial role in the dynamic tensile process and have little effect on the quasi-static tensile process. In the quasi-static tensile process, the only obstacle to dislocation motion is the obstacle related to the dislocation structure itself [11]. Therefore, nano-twin boundaries should be considered in the analysis of high strain rate tension, and the average free path, Λ, can be calculated by the following:

$$\frac{1}{\wedge}=\frac{1}{d}+k_1\sqrt{\rho} \tag{12}$$

$$\frac{1}{\wedge}=\frac{1}{d}+\frac{i_t}{t}+k_1\sqrt{\rho} \tag{13}$$

where, d is the average grain size of the sample, which is 21.8 μm; k_1 is a non-thermal hardening factor, take 0.018 [54]; i_t is the ratio constant of twin spacing, take 0.14 [54]; according to the statistical results of TEM. At room temperature, the average twin thicknesses at strain rates of 1,600 s^{-1} and 2,000 s^{-1} were 31.2 nm and 19.5 nm, respectively. At low temperature, the average twin thicknesses at strain rates of 1,000 s^{-1}, 1,600 s^{-1}, and 2,000 s^{-1} were 32.4 nm, 25.5 nm, and 16.1 nm, respectively.

By substituting the corresponding parameters into the above formula, the variation of the flow stress with strain at room temperature was successfully fitted. The fitting results were shown in Fig. 16(a). At the same time, the change of the flow stress with strain at 77 K was further predicted. It was worth noting that many parameters in the above formula will vary with temperature. For example, the shear modulus, G, is a temperature-dependent constant that increases with decreasing temperature. Due to the limited reports on the $Fe_{40}Mn_{20}Cr_{20}Ni_{20}$ HEA, there is a lack of research on the temperature sensitivity of shear modulus, *G*. The shear modulus, *G*, of the $Fe_{40}Mn_{20}Cr_{20}Ni_{20}$ at 77 K is considered to be 1.1 times that at 298 K, namely 93.5 GPa [55]. Obviously, the current constitutive model well predicted the change of the flow stress with strain at low temperature (77 K), and the fitting results were shown in Fig. 16(b). Table 4 listed the values of the relevant parameters in the Z-A model and the Taylor model.

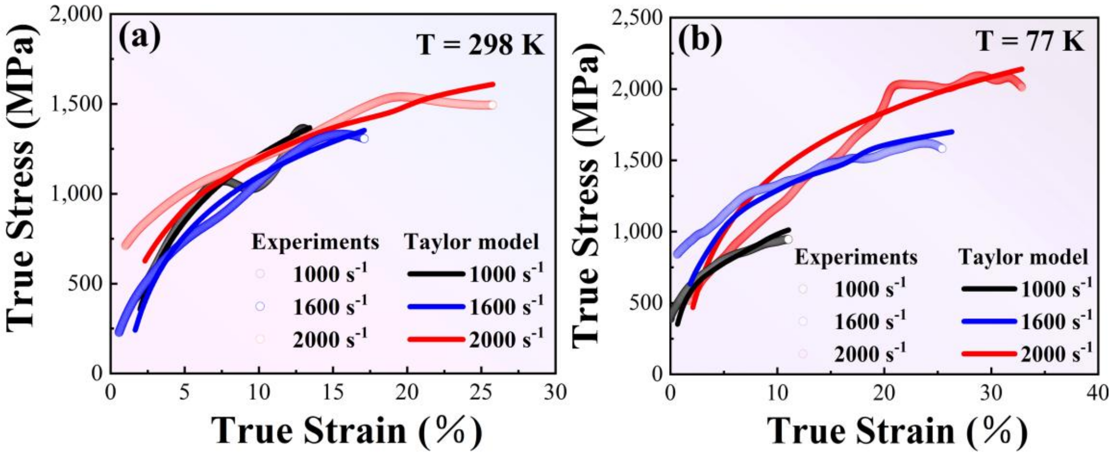

Fig. 16 The experimental data of the $Fe_{40}Mn_{20}Cr_{20}Ni_{20}$ HEA at room temperature and low temperature and the fitting results of Taylor model. The black curve is 1,000 s^{-1}; the blue curve is 1,600 s^{-1}; the red curve is 2,000 s^{-1}

Table 4 Material parameters used in Z-A thermal activation model and Taylor model

Sign	Implication	Numerical value	
		Room temperature	Low temperature
σ_0^*	thermal stress	396 MPa	
σ_g	grain boundary strengthening	106 MPa	
β_0	material constant	2.2×10^{-3} /K	
β_1	material constant	2.0×10^{-4} /K	
c	material constant	4.98×10^{-4} s	
M	Taylor factor	3.06	3.06
G	shear modulus	85 GPa	93.5 GPa
b	burgers vector	0.255 nm	0.255 nm
C_v	heat capacity	0.454 J/g K	0.454 J/g K
β	plastic energy-thermal energy conversion fraction	0.9	0.9
ρ	density	7.90 g/cm^{-3}	7.90 g/cm^{-3}
γ_{SF}	stacking fault energy	42.8 mJ/m^2	14.6 mJ/m^2
K	Boltzmann's constant	1.38×10^{-23}	1.38×10^{-23}
A	material constant	4.9×10^{-18} J	5.6×10^{-18} J
$\dot{\varepsilon}_0$	reference strain rate	10^7 s^{-1}	10^7 s^{-1}
k_0	adiabatic recovery factor	36.88	4.60
k_1	no thermal hardening factor	0.018	0.018
i_t	proportional constant of twin spacing	0.14	0.14

4.3 Effect of dislocations and twins on mechanical properties of the HEA

During the dynamic tensile process, a large number of dislocations and deformation twins with different morphologies were generated in the current HEA. With the increase of strain rate, the dislocation distribution was more uniform, and the proportion of high-density dislocations was more, as shown in Figs. 10 and 11. ~~In the process of dynamic tensile loading, the instantaneous high stress causes the dislocation movement to start rapidly, which leads to the increase of the rate and energy level of dislocation movement, the shortening of the dislocation spacing, and the generation of dislocation lines in the grains. These dislocation lines cross each other to form high-~~

~~density dislocation lines.~~ During the impact loading process, the dislocation lines cross each other to form high-density dislocations. At the same time, this trend will also lead to an increase in the Peierls-Nabarro force (P-N), which is the shear stress required to induce slip, thereby increasing the critical shear stress of slip and producing a strengthening effect on HEAs [56]. At the same time, with the increase of strain rates, dislocations do not have enough time to slip to grain boundaries and disappear, which promotes the accumulation of dislocations [57].

The main deformation mechanisms of the $Fe_{40}Mn_{20}Cr_{20}Ni_{20}$ HEA at high strain rates are dislocations and twins. During the deformation process, high-density dislocations make HEA exhibit better work-hardening ability. However, a high dislocation density usually limits the movement of dislocations and induces dislocation accumulation, resulting in a serious decrease in the plasticity of the HEA at high strain rates, yielding a strength-plastic trade-off dilemma [41,58]. On the other hand, by forming additional twin boundaries, deformation twins hinder dislocation movement, increase dislocation storage capacity, improve the strength of the alloy, and delay the occurrence of necking without significantly sacrificing plasticity [59]. At the same time, at high strain rates, due to the activation of instantaneous high flow stresses, deformation twins are more easily activated than quasi-static, reducing the average free path of deformation and enhancing the strengthening ability of dislocations [60]. In general, deformation twins are determined by the generation of SFE and grain size. Lower SFE and larger grain size will reduce the twin stress [61]. SFE mainly triggers the formation of deformation twins, resulting in twin-induced plasticity (TWIP) [60].

Compared with room temperature dynamic tension, the $Fe_{40}Mn_{20}Cr_{20}Ni_{20}$ HEA under low temperature dynamic tension produced higher-density dislocations and twins in two different directions, as presented in Fig. 13. In general, dislocation slip is difficult at low temperatures, and high strain rates do not provide sufficient time for dislocation slip, resulting in a local concentration of dislocations and decreased plasticity [62,63]. However, the SFE of the alloy decreases with the decrease of temperature, which increases the flow stress. At the same strain rate, more deformation twins are formed to improve the strength and plasticity of HEAs [64]. At the same time, a large number of deformation twin boundaries refine the grains and provide significant grain-boundary strengthening [65]. It is reported that the samples under low temperature dynamic loading show higher energy absorption than the samples under room temperature dynamic loading [56]. ~~The change trend of energy absorption with strain rate and temperature is consistent with the yield strength. With the increase of strain rate, the flow stress and plasticity will increase, so as to improve the yield strength and increase energy absorption without affecting the plasticity. Therefore, it is believed that increasing the strain rates and decreasing the temperatures have similar effects on promoting deformation twinning.~~ The synergistic effect of deformation twins and dislocation slip is the key to the simultaneous improvement of strength and plasticity of the HEA under dynamic tension.

In order to more intuitively express the microstructure evolution mechanism of the $Fe_{40}Mn_{20}Cr_{20}Ni_{20}$ high-entropy alloy after dynamic stretching, a schematic diagram is shown in Fig. 17. The microstructure of the deformed HEA was mainly composed of deformation twins (DTs) and dense dislocations, including dislocation lines, dislocation cells (DCs), dislocation tangles, and high-density dislocation walls (HDDWs). At low strain rates, the deformation mechanism of the alloy after dynamic stretching was still dominated by dislocation slip. With the increase of strain rate, the deformation twins were activated, which became the main mechanism of plastic deformation of the HEA at high strain rates. At low temperature, some deformation twins were also produced in the alloy after 1,000 s^{-1} strain rate deformation. With the increase of strain rate, there were two kinds of deformation twins in different directions, and a large number of dislocations were piled up at the intersection of twins, which improves the work-hardening ability of the HEA. Therefore, under dynamic tension, the interaction of different forms of dislocations and twins makes the strength and plasticity of the alloy increase simultaneously.

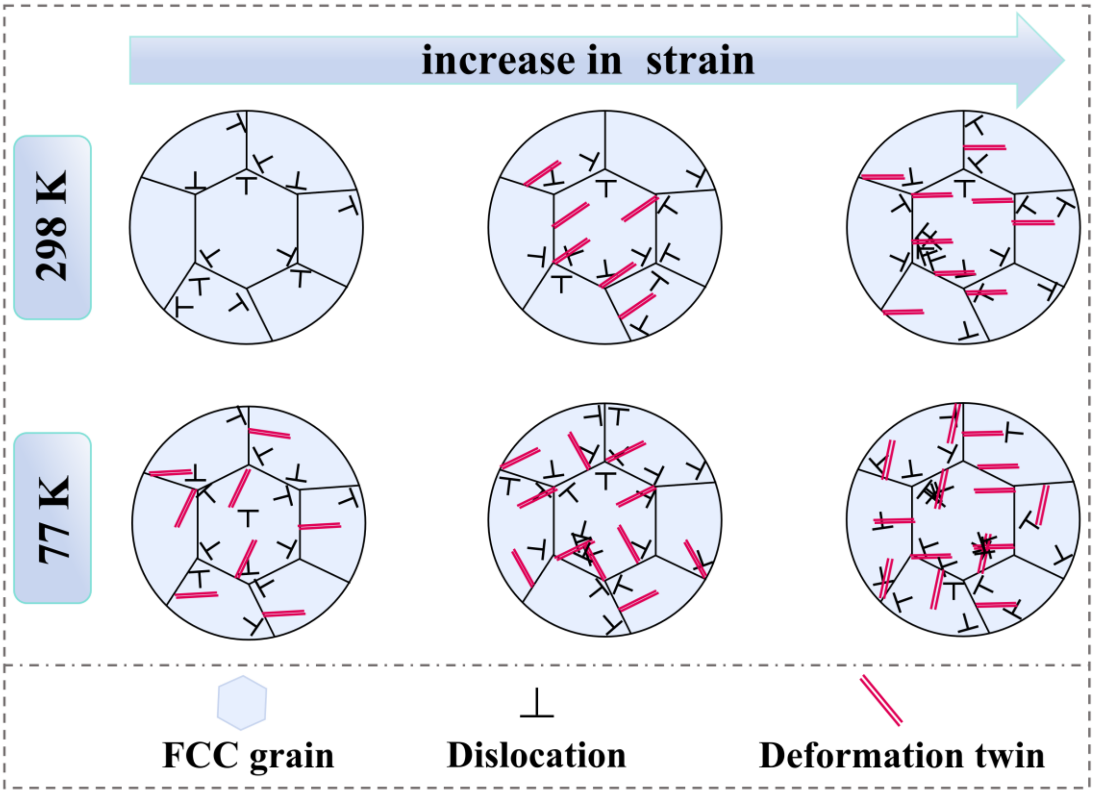

Fig. 17 The schematic diagram of the microstructure evolution of the alloy after dynamic

stretching

5. Conclusions

In this study, the mechanical properties of the $Fe_{40}Mn_{20}Cr_{20}Ni_{20}$ HEA prepared by industrialization at different temperatures (77 K – 1,073 K) and different strain rates (1,000 s^{-1}, 1,600 s^{-1} lead and 2,000 s^{-1}) were systematically analyzed. The mechanical properties and deformation damage mechanisms of the alloy at room temperature and low temperature were studied. The classical Z-A thermally activated constitutive model and Taylor model were used to successfully fit the yield strength and flow stress changes of the alloy under different states. The following main conclusions are drawn:

(1) Under high temperature tension, the alloy shows a particularly obvious softening phenomenon at 873 K, and the strength and plasticity are significantly reduced. Under low temperature quasi-static tension, the current HEA exhibits an excellent combination of strength and plasticity. At 10^{-3} s^{-1}, ~~compared with the quasi-static state at room temperature, the yield strength and plasticity of the alloy at low temperature can reach 405 MPa and 97.5%, which are increased by about 78% and 124%, respectively~~. compared with the quasi-static state at room temperature, the yield strength and plasticity of the alloy at low temperature are increased by about 78% and 124%, which can reach 405 MPa and 97.5%, respectively. With the increase of strain rate, the yield strength of the alloy can reach up to 481 MPa, and the plasticity is still as high as 95%.

(2) At room temperature, the yield strength of the alloy is increased by about 97% and the elongation is maintained at a high level (25.3%) when the strain rate is 1,000 s^{-}

^{1} compared with the quasi-static tensile loading. With the increase of strain rate, the yield strength of the alloy can reach 995 MPa, and the plasticity is as high as 44.5%. At low temperature, the yield strength of the alloy is up to 1,120 MPa and the plasticity is 45.7%.

(3) During the dynamic tensile process, the interaction of different forms of dislocations and deformation twins together improves the strength and work-hardening ability of the $Fe_{40}Mn_{20}Cr_{20}Ni_{20}$ HEA. At room temperature of 1,000 s^{-1}, the deformation mechanism is still dominated by dislocation slip. With the increase of strain rate and the decrease of temperature, a large number of deformation twins are activated, which seriously hinders the dislocation movement and improves the work-hardening ability.

(4) The temperature sensitivity and strain-rate sensitivity of the yield strength of the alloy were successfully predicted using the classical Z-A thermal-activation constitutive model, and the fitting results were good. At the same time, the Taylor model related to the flow stress was used to predict the change of the flow stress of the alloy under dynamic tension. The model was applied to the low temperature dynamic loading, and the fitting results were basically consistent with the experimental results. Finally, the excellent mechanical properties of the $Fe_{40}Mn_{20}Cr_{20}Ni_{20}$ HEA under dynamic loading are expected to become a candidate material for impact resistant structural materials.

Acknowledgement

Junwei Qiao would like to acknowledge the support of the National Natural Science Foundation of China (No. 52271110) and the Taiyuan Key Core Technology Tackling Project (Open Bidding for Selecting the Best Candidates, No. 2024TYJB0113).

Date availability

The raw data related to this manuscript would be made available on request.

References

[1] Cantor B, Chang I T H, Knight P, et al. Materials Science and Engineering: A, 2004, 375-377: 213-218.

[2] Yeh J W. JOM, 2015, 67(10): 2254-2261.

[3] George E P, Curtin W A, Tasan C C. Acta Materialia, 2020, 188: 435-474.

[4] Liu J P, Chen J X, Liu T W, et al. Scripta Materialia, 2020, 181: 19-24.

[5] Tang Y, Li D Y. Science Advances, 2022, 8(32): eabp9096.

[6] Joseph J, Haghdadi N, Annasamy M, et al. Scripta Materialia, 2020, 186: 230-235.

[7] Li S, Liu X, Hou X, et al. Journal of Materials Research and Technology, 2025, 35: 4142-4163.

[8] Yang R, Li F, Huang Z, et al. Tribology International, 2024, 200: 110084.

[9] Dannemann K A, Chalivendra V B, Song B. Experimental Mechanics, 2012, 52(2): 117-118.

[10] Tang Y, Wang R, Xiao B, et al. Progress in Materials Science, 2023, 135: 101090.

[11] Wang K, Jin X, Zhang Y, et al. Physical Review Materials, 2021, 5(11): 113608.

[12] Zhang Q, Peng S Y, Tian Y Z. Materials Science and Engineering: A, 2024, 900: 146494.

[13] Zhang C, Han B, Shi M. Journal of Molecular Modeling, 2023, 29(4): 104.

[14] Deng H W, Ge H E, Zhan C Y, et al. Journal of Materials Research and Technology, 2023, 24: 9731-9742.

[15] He Z F, Jia N, Ma D, et al. Materials Science and Engineering: A, 2019, 759: 437-447.

[16] Guo Z, Jing S, Yu M, et al. Materials Characterization, 2024, 217: 114328.

[17] Xie L, Wu G, Peng Q, et al. Materials Today Communications, 2023, 37: 107264.

[18] Gao X, Liu J, Fu W, et al. Materials & Design, 2023, 233: 112250.

[19] Gali A, George E P. Intermetallics, 2013, 39: 74-78.

[20] Zheng R, Gong W, Du J ping, et al. Acta Materialia, 2022, 238: 118243.

[21] Fu A, Cao Y, Zhou Z, et al. Materials Today Communications, 2024, 38: 108558.

[22] Wang J, Liu B, Zhou H, et al. Intermetallics, 2024, 175: 108532.

[23] Bian B B, Guo N, Yang H J, et al. Journal of Alloys and Compounds, 2020, 827: 153981.

[24] Cao T, Zhang Q, Wang L, et al. Acta Materialia, 2023, 260: 119343.

[25] Yang Z, Yang M, Ma Y, et al. Materials Science and Engineering: A, 2020, 793: 139854.

[26] Xiao Y, Kozak R, Haché M J R, et al. Materials Science and Engineering: A, 2020, 790: 139429.

[27] Pu Z, Chen Y, Dai L H. Materials Science and Engineering: A, 2018, 736: 156-166.

[28] Jiang Z J, He J Y, Wang H Y, et al. Materials Research Letters, 2016, 4(4): 226-232.

[29] Zhang T W, Ma S G, Zhao D, et al. International Journal of Plasticity, 2020, 124: 226-246.

[30] Wang Y Z, Jiao Z M, Bian G B, et al. Materials Science and Engineering: A, 2022, 839: 142837.

[31] Gao X, Chen R, Liu T, et al. Journal of Materials Science, 2022, 57(12): 6573-6606.

[32] Shih M, Miao J, Mills M, et al. Nature Communications, 2021, 12(1): 3590.

[33] León-Cázares F D, Schlütter R, Monni F, et al. Acta Materialia, 2022, 241: 118372.

[34] Wang S, Liu K, Wang Z, et al. Materials Science and Engineering: A, 2024, 901: 146583.

[35] Wang J, Liu Y, Liu B, et al. Materials Science and Engineering: A, 2017, 689: 233-242.

[36] Li S, Li S, Liu L, et al. Materials Science and Engineering: A, 2023, 877: 145160.

[37] Li Z M, Li X N, Hu Y L, et al. Acta Materialia, 2021, 203: 116458.

[38] Curtze S, Kuokkala V T. Acta Materialia, 2010, 58(15): 5129-5141.
[39] Laplanche G, Kostka A, Horst O M, et al. Acta Materialia, 2016, 118: 152-163.
[40] Li W, Xie D, Li D, et al. Progress in Materials Science, 2021, 118: 100777.
[41] Qiao Y, Chen Y, Cao F H, et al. International Journal of Impact Engineering, 2021, 158: 104008.
[42] Chen G, Li L T, Qiao J W, et al. Materials Letters, 2019, 238: 163-166.
[43] Qi L, Huang X D, Zhang A P, et al. Scripta Materialia, 2021, 201: 113929.
[44] Paul S, Bhattacharjee P P. Materials Today Communications, 2024, 38: 107678.
[45] Meyers M A. Dynamic Behavior of Materials[M]. 1st ed. Wiley, 1994.
[46] Zerilli F J, Armstrong R W. Journal of Applied Physics, 1987, 61(5): 1816-1825.
[47] Otto F, Dlouhý A, Somsen Ch, et al. Acta Materialia, 2013, 61(15): 5743-5755.
[48] Zerilli F J, Armstrong R W. Acta Metallurgica et Materialia, 1992, 40(8): 1803-1808.
[49] Guo W G, Nemat-Nasser S. Mechanics of Materials, 2006, 38(11): 1090-1103.
[50] Lee J I, Oh H S, Park E S. Applied Physics Letters, 2016, 109(6): 061906.
[51] Hutchinson B, Ridley N. Scripta Materialia, 2006, 55(4): 299-302.
[52] Laplanche G, Kostka A, Horst O M, et al. Acta Materialia, 2016, 118: 152-163.
[53] Kocks U F, Mecking H. Progress in Materials Science, 2003, 48(3): 171-273.
[54] Liang Z Y, Wang X, Huang W, et al. Acta Materialia, 2015, 88: 170-179.
[55] Wu Z, Bei H, Pharr G M, et al. Acta Materialia, 2014, 81: 428-441.
[56] Huang G, Li B, Chen Y, et al. Journal of Materials Science & Technology, 2024, 183: 241-257.
[57] Wang L, Qiao J W, Ma S G, et al. Materials Science and Engineering: A, 2018, 727: 208-213.
[58] He B B, Hu B, Yen H W, et al. Science, 2017, 357(6355): 1029-1032.
[59] Gao P, Ma Z, Gu J, et al. Science China Materials, 2022, 65(3): 811-819.
[60] Jiang W, Gao X, Guo Y, et al. Materials Science and Engineering: A, 2021, 824: 141858.
[61] Mengiste B T, Arab A, Guo Y, et al. Journal of Alloys and Compounds, 2024, 980: 173627.
[62] Zhang Y, Zuo T T, Tang Z, et al. Progress in Materials Science, 2014, 61: 1-93.
[63] Gao X, Lu Y, Zhang B, et al. Acta Materialia, 2017, 141: 59-66.
[64] Zhao B, Huang P, Zhang L, et al. Scientific Reports, 2020, 10(1): 3086.
[65] Jiang K, Ren T, Shan G, et al. Materials Science and Engineering: A, 2020, 797: 140125.